MID-AMERICA
TRANSPORTATION CENTER

Report # MATC-UI: 220

Final Report
WBS: 25-1121-0003-220

University of Nebraska Lincoln
K-STATE Kansas State University
KU The University of Kansas
Missouri S&T University of Science & Technology
Lincoln University
University of Missouri
Iowa State University
The University of Iowa

Diagnosis of Retrofit Fatigue Crack Re-Initiation and Growth in Steel-Girder Bridges for Proactive Repair and Emergency Planning

Salam Rahmatalla, Ph.D
Associate Professor
Civil and Environmental Engineering
University of Iowa

Charles Schallhorn, M.S.
Research Assistant

The University of Iowa

2014

A Coopertative Research Project sponsored by
U.S. Department of Tranportation-Research, Innovation and Technology Innovation Administration

MATC

Diagnosis of Retrofit Fatigue Crack Re-Initiation and Growth in Steel-Girder Bridges for Proactive Repair and Emergency Planning

Salam Rahmatalla, Ph.D
Associate Professor
Civil and Environmental Engineering
University of Iowa

Charles Schallhorn, M.S.
Research Assistant
Civil and Environmental Engineering
University of Iowa

A Report on Research Sponsored by

Mid-America Transportation Center

University of Nebraska-Lincoln

July 2014

Technical Report Documentation Page

1. Report No. 25-1121-0003-220	2. Government Accession No. 01487967	3. Recipient's Catalog No.
4. Title and Subtitle Diagnosis of retrofit fatigue crack re-initiation and growth in steel-girder bridges for proactive repair and emergency planning		5. Report Date July 2014
		6. Performing Organization Code
7. Author(s) Salam Rahmatalla, Charles Schallhorn		8. Performing Organization Report No. 25-1121-0003-220
9. Performing Organization Name and Address Mid-America Transportation Center 2200 Vine St. PO Box 830851 Lincoln, NE 68583-0851		10. Work Unit No. (TRAIS)
		11. Contract or Grant No. Contract ID DTRT12-G-UTC07
12. Sponsoring Agency Name and Address Research and Innovative Technology Administration 1200 New Jersey Ave., SE Washington, D.C. 20590		13. Type of Report and Period Covered December 2013 – July 2014
		14. Sponsoring Agency Code MATC TRB RiP No. 34765
15. Supplementary Notes		

16. Abstract

This report presents a vibration-based damage-detection methodology that is capable of effectively capturing crack growth near connections and crack re-initiation of retrofitted connections. The proposed damage detection algorithm was tested using numerical simulation and laboratory experimentation. Finite element models of the initial and retrofitted connections were developed to investigate the effect of crack growth before and after circular holes were implemented as stress relief measures. Laboratory experimentation on retrofitted specimens showed a tendency for the crack to branch in different directions in lieu of re-initiating through the holes. Throughout both the numerical and laboratory analyses, the results were able to successfully detect damage by calculating a damage indicator, as specified within the algorithm. Although it was beyond the initial scope of the presented work, it was observed that the damage indicator also provides a relative quantification of the damage severity, i.e., as damage increased in the specimen, the magnitude of the damage indicator increased monotonically.

17. Key Words Deterioration; Fatigue cracking; Finite element method; Girder bridges; Inspection; Repairing; Retrofitting; Steel bridges	18. Distribution Statement

19. Security Classif. (of this report) Unclassified	20. Security Classif. (of this page) Unclassified	21. No. of Pages 39	22. Price

Table of Contents

List of Figures

Acknowledgements

The authors would like to thank Guandong Qiao and Samer Al Jailawi for their assistance with the data collection process. Also, appreciation is given to Steve Struckman, Bill Jennings, and Brandon Barquist for fabricating the steel specimens.

Disclaimer

Abstract

This report presents a vibration-based damage-detection methodology that is capable of effectively capturing crack growth near connections and crack re-initiation of retrofitted connections. The proposed damage detection algorithm was tested using numerical simulation and laboratory experimentation. Finite element models of the initial and retrofitted connections were developed to investigate the effect of crack growth before and after circular holes were implemented as stress relief measures. Laboratory experimentation on retrofitted specimens showed a tendency for the crack to branch in different directions in lieu of re-initiating through the holes. Throughout both the numerical and laboratory analyses, the results were able to successfully detect damage by calculating a damage indicator, as specified within the algorithm. Although it was beyond the initial scope of the presented work, it was observed that the damage indicator also provides a relative quantification of the damage severity, i.e., as damage increased in the specimen, the magnitude of the damage indicator increased monotonically.

Chapter 1 Introduction and Background

Thousands of old multiple-steel-girder bridges were built in the United States and are vulnerable to fatigue cracking (Connor and Fisher, 2006; Fisher, 1997; Al-Emrani and Kliger, 2009; Lu et al., 2010). Fatigue cracking normally occurs due to poor detailing and out-of-plane relative displacement mostly in the web area of the girder-diaphragm connections (Liu, et al, 2010). The implementation of retrofits to stop fatigue crack growth in steel-girder bridges has shown variable success (Wipf et al., 2003). The stop-holes (Grondin and Kulak, 2010) retrofit, where holes are drilled at the tips of existing cracks, has been customarily adopted by many Departments of Transportation across the U.S. as a common repair practice for highway bridges (USDOT, 2013). While stop-holes are an effective method to stop fatigue crack growth, the choice of stop-hole sizes and locations relative to the crack tips may only temporarily hinder the propagation of the crack, leading to re-initiation (Cousins et al., 1998). Indeed, field studies (Wipf et al., 1998; Tarries et al., 2002) have shown the tendency of some of these cracks to re-initiate around the stop-holes, which can potentially cause a real danger to the integrity and safety of the bridges. Figure 1.1 depicts a common fatigue crack that occurs in steel-girder bridges, near the gap between the diaphragm (crossframe) and the girder web. Figure 1.2 also depicts this type of fatigue crack and shows a stop-hole retrofit with crack re-initiation.

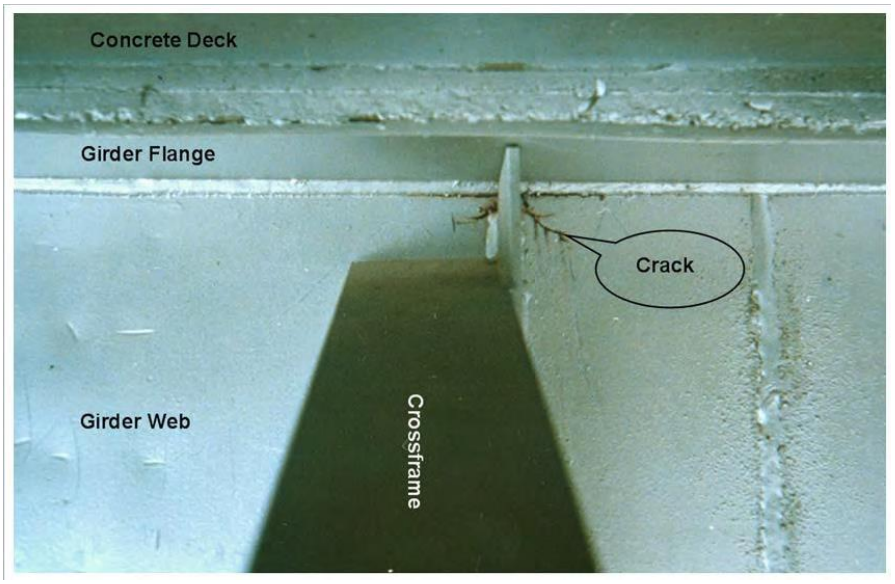

Figure 1.1 Fatigue crack formed in web gap of highway steel-girder bridge. Figure from FHWA Publication No. FHWA-IF-13-020

Figure 1.2 Retrofitted fatigue crack of highway steel-girder bridge with re-initiation. Figure from FHWA Publication No. FHWA-IF-13-020

With these common failures in mind, there is a critical and urgent need for a methodology that can detect cracks' growth and re-initiation in critical regions of the bridge, so that repair planners can take the appropriate repair measures. Fatigue cracks can grow quickly and cause unexpected damage before the traditional biennial inspection can take place. Therefore, it is critical to continually monitor fatigue crack re-initiation at retrofitted connections to help emergency responders and repair planners determine the action that has to be taken. High-stress areas on structures are normally located using a finite element model of the structure. This process could present general information about the stress distribution at different locations on the bridge; still, it may be impractical for most of the existing/old structures due to changes in the static/dynamic characteristics of the structure caused by environmental effects such as erosion, corrosion, settlement, and so forth. Therefore, there is a need to install appropriate sensors and implement a damage-detection algorithm to identify any changes in the static/dynamic behavior of the structure during its lifetime operations, without heavily depending on the initial engineering drawings of the bridge.

Vibration-based damage detection and health monitoring methodologies have become more popular during the last two decades (Doebling et al., 1998; Yan et al., 2007; Chesne and Deraemaeker, 2013). One main reason behind this popularity is in these methods' effectiveness in capturing the changes in the dynamic response of the structure due to changes in the stiffness, mass, and damping properties that can result from damage. Many vibration-based methodologies have been introduced, such as those based on the changes in modal parameters, the frequency response function, and their curvatures, with the capability of sensing global changes in the structural behavior. However, due to difficulties associated with accurately measuring excitation forces and predicting modal parameters, their use in field applications has been limited. On the other hand, interest in using the transmissibility function for damage detection has greatly increased over the past decade (Maia et al., 2011; Devriendt and Guillaume, 2008; Johnson and Adams, 2002; Li and Hao, 2013) as it overcomes the need for input force measurement or subsequent modal parameter calculations. Transmissibility is calculated from the response ratio between two degrees of freedom and is expected to be more sensitive to local changes in the dynamic characteristics of a structural system between these degrees of freedom than the frequency response function (FRF) (Maia et al., 2011).

In this work, a damage detection algorithm that is capable of identifying crack growth and re-initiation near connections is presented. Chapter 2 outlines the methodology and clarifies all the necessary background information. The entire collection of analyses used within this work are detailed in chapter 3, with the numerical analysis in section 3.1 and the laboratory analysis in section 3.2. The setup, testing procedures, results, and discussions for the numerical analyses are described in sections 3.1.1 – 3.1.3, and sections 3.2.1 – 3.2.3 describe these same topics for the laboratory analyses. Concluding remarks are presented in chapter 4.

Chapter 2 Damage Detection Algorithm

In this chapter, the proposed vibration-based damage detection algorithm is introduced. This procedure adds novel aspects to data analysis in pursuit of an accurate localized vibration-based damage detection algorithm that could be implemented in numerous environments.

2.1 Nomenclature

For purposes of clarification, an account of the data used within this algorithm as well as the terminology used to describe this data must be given. All of the experimentation completed in this work was based on *impact testing* in which the response due to an impulse loading of the structure was measured. Each response's acceleration time-history (up to two seconds) shall be further referred to as a single *impact*. Two sets of data shall be referred to in the discussion of the damage detection algorithm: *baseline set* and *comparison set*. The *baseline set* is a collection of a prescribed number of impacts (N) monitoring the state of the structure with which other states will be compared. One impact was required for the numerical analysis, while twenty impacts were required for the experimental analyses. Similarly, the *comparison set* is the collection of a number of subsequent impacts (M) (one for the numerical analysis and twenty for the experimental analyses) for which the state of the structure could be damaged or remain at the same state as the baseline set. To give a numerical value to the damage detection, a *damage indicator* will be used. This damage indicator will be a comparable representation of each of the data sets so that damage detection can be objectively identified.

2.2 Algorithm

A detailed description of the damage detection algorithm will be given in this section. The procedure is outlined in figure 2.1.

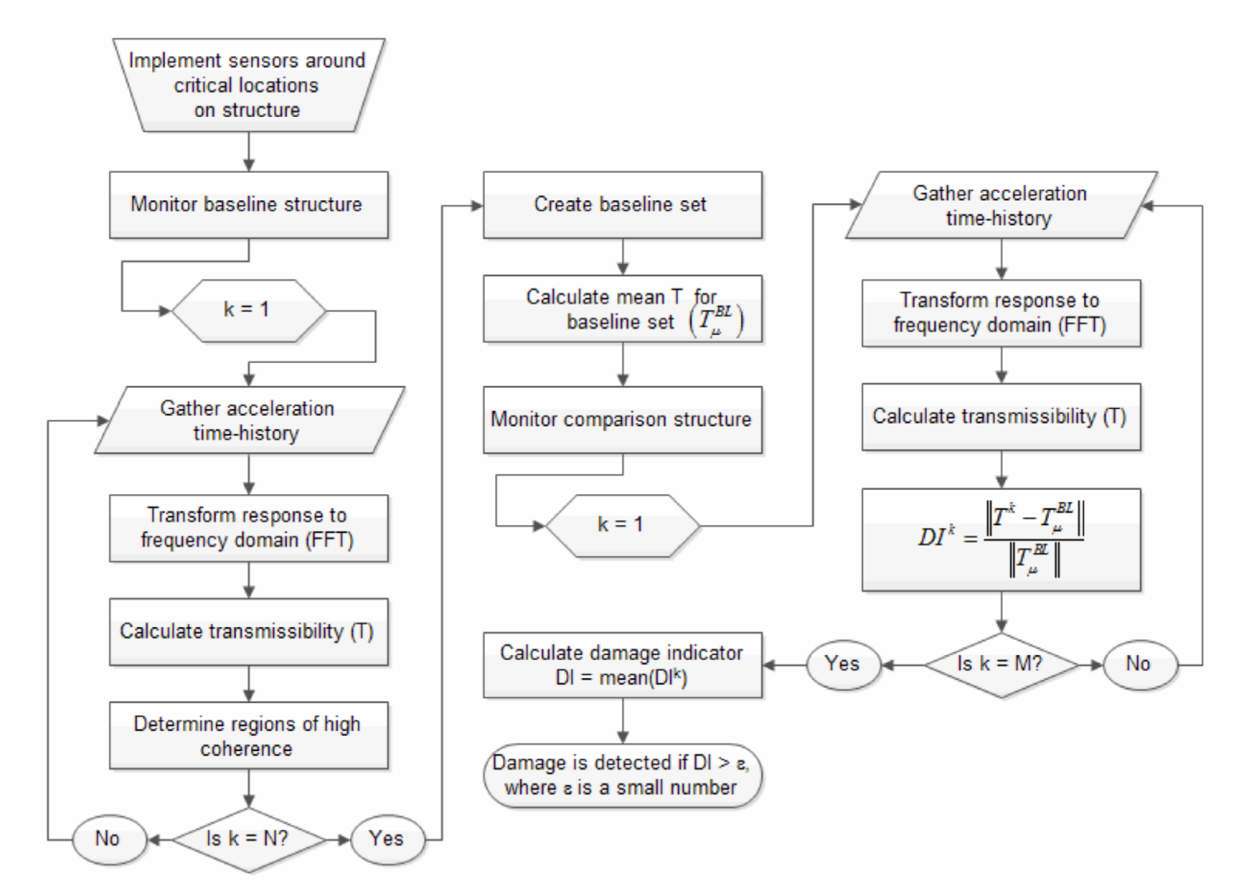

Figure 2.1 Outlined procedure for vibration-based damage detection algorithm

The algorithm starts at the upper left corner of figure 2.1 with implementing the sensors around critical prone-to-damage locations, such as connections and high stress areas. By installing the sensors around these damage-critical zones, the capacity for detecting small deficiencies is expected to be increased, thus directly localizing the damage detection algorithm. Work has been completed (Devriendt and Guillaume, 2008; Maia,et al., 2011) concluding that transmissibility (**T**) is expected to be more sensitive to local changes between the degrees of freedom from which **T** is calculated, thus warranting the decision to implement the sensors near damage-critical locations.

Throughout this work, the acceleration time-histories were collected based on an impact loading scenario. The data files measure the acceleration both during and after the impact, consequently measuring the forced, transitional, and transient responses of the structural system.

The impact (acceleration response time history) is then transformed to the frequency domain using a fast-Fourier transform (FFT). Furthermore, **T** is calculated by using equation 2.1.

$$\mathbf{T}_{ij}(\omega) = 20\log_{10}\frac{\boldsymbol{X}_i(\boldsymbol{\omega})}{\boldsymbol{X}_j(\boldsymbol{\omega})} \tag{2.1}$$

Where,

$\boldsymbol{X}_i$ is the response in the frequency domain at location i

$\boldsymbol{X}_j$ is the response in the frequency domain at location j.

The units of **T** are calculated as decibel (dB) in order to more easily observe small changes in the dynamic characteristics of the structure.

The decision process for detecting damage is based on changes to **T**, and it has been indicated that **T** is more efficient when limited to certain frequency bands when detecting damage (Thyagarajan et al., 1998). Also, one can increase the accuracy of the decision process by limiting these bands (Chesne and Deraemaeker, 2013). Although these works have not offered evidence for how to limit the frequency bands, the current work proposes using the coherence between sensor signals.

Coherence is a powerful tool commonly used in signal processing to determine the linearity between two signals and assess measurement quality. This relationship to determine the frequency ranges in which the signals behave linearly is determined by equation 2.2.

$$\gamma_{ij}(\omega) = \frac{\left|S_{ij}(\omega)\right|^2}{S_{ii}(\omega) S_{jj}(\omega)} \tag{2.2}$$

Where,

γ_{ij} is the coherence between sensors at locations i and j

S_{ij} is the cross-spectral density between sensors at locations i and j

S_{ii} is the auto-spectral density of the sensor at location i

S_{jj} is the auto-spectral density of the sensor at location j

The values of coherence range from zero to one, with ideal linear signals resulting in a unit value of coherence.

The statistical method used in this algorithm is the calculation of the mean signal for the baseline set, which is then used in the calculation of the damage indicator. The damage indicator is calculated by normalizing the difference between **T** of each comparison impact and **T** of the mean baseline impact for a given frequency range Ω, as shown in equation 2.3,

$$DI = \frac{1}{M} \sum_{D=1}^{M} \frac{\left\| \boldsymbol{T}^{D}(\Omega) - \boldsymbol{T}_{\mu}^{BL}(\Omega) \right\|}{\left\| \boldsymbol{T}_{\mu}^{BL}(\Omega) \right\|} \tag{2.3}$$

Where,

$\boldsymbol{T}^{D}(\Omega)$ is the transmissibility for the comparison impacts over the frequency range Ω,

$\boldsymbol{T}_{\mu}^{BL}(\Omega)$ is the mean transmissibility for the baseline impacts over the frequency range Ω, and

M is the number of impacts used in the comparison set.

The frequency range Ω was chosen based on the regions of high coherence.

The damage indicator produces a positive scalar value to be used as a comparable measure for detecting damage. For an ideal system without noise, when comparing the same damage state as the baseline, the damage indicator should produce a value of zero. Changes to the structural dynamics of the system, i.e., damage, will then increase the damage indicator.

Chapter 3 Analysis

Figure 3.1 is a schematic that shows the layout and dimensions of the connection specimen that was designed for use in the entirety of the completed work. This model was inspired by the sacrificial specimen used by Iowa State University (Phares et al., 2013) to represent a girder-diaphragm connection that is common in steel girder bridges. The comparison between the connection and the analytical model is shown in figure 3.2.

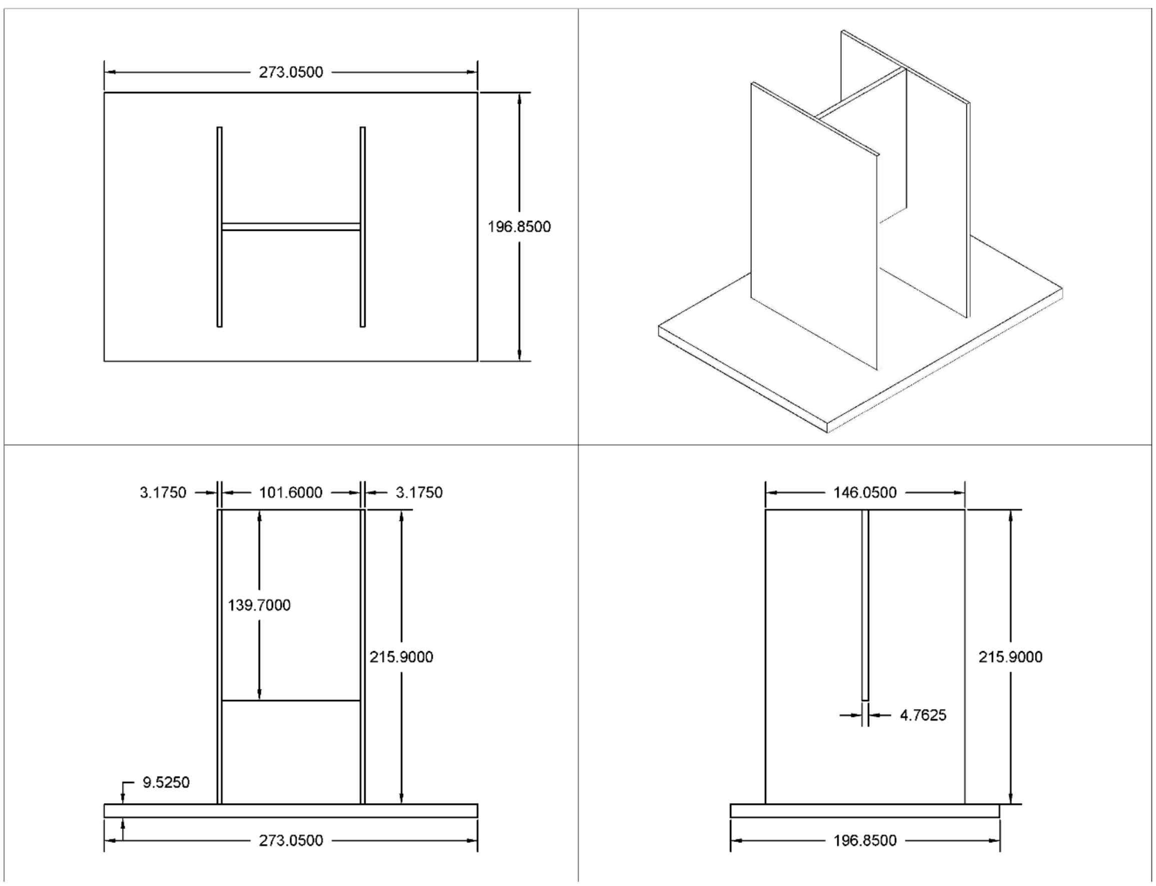

Figure 3.1 Layout and dimensions of specimen used for all analyses (all units are *mm*)

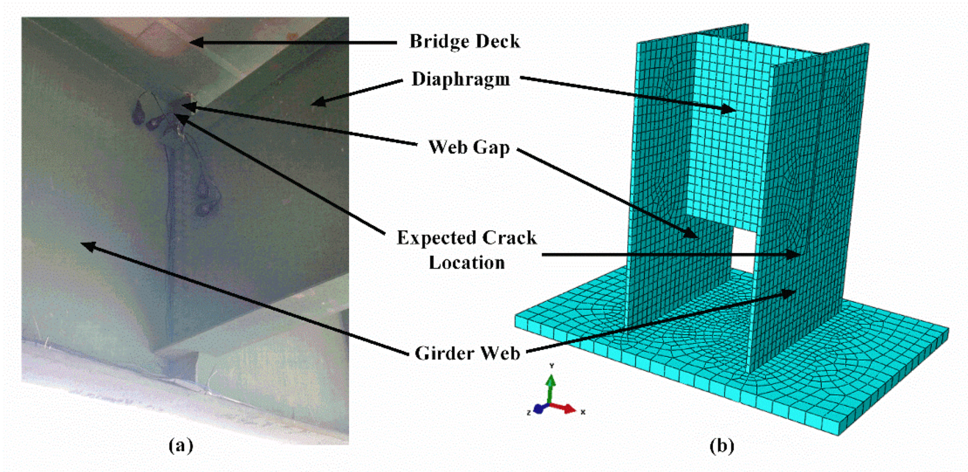

Figure 3.2 Representative model of the connection between the web of the girder and the diaphragm, (a) real bridge, (b) finite element model.

3.1 Numerical Analysis

A numerical analysis was completed in order to investigate the capabilities of the damage detection algorithm on a relatively complex structure, such as a connection. This analysis was completed using a commercially available finite element program (ABAQUS 6.12, Dassault Systemes Simulia Corp.) in which the output acceleration data, resulting from a single impact loading, was exported into Matlab (MATLAB R2013a, The MathWorks Inc.) for use in the damage detection algorithm.

3.1.1 Numerical Setup

The finite element model of the specimen was created in ABAQUS using general modeling techniques. The mesh created for the numerical model consisted of approximately 3500 20-noded quadratic brick elements. Figure 3.3(a) depicts the layout of the numerical model, the locations of the crack and the force, as well as the labels for the nodes (locations) used for monitoring the response of the system. The accelerations at all nodes were measured in a direction parallel to the direction of loading. Figure 3.3(b-d) depicts the meshing of the pseudo-girder web for the healthy state (D0) as well as the crack for the two damage states (D1, D2). Figure 3.3(e-g) shows the respective stress contour plots for the healthy state and each of the damage states. A red-to-blue color map was used to depict high-stress contours in red and low-stress contours in blue. Damage was introduced manually by modeling a seam crack at the specified locations, in which the seam crack was through the entire thickness of the pseudo-girder web. The crack was modeled as jagged to simulate a more realistic cracking scenario. The first damaged state (D1) has a 25.4 mm jagged crack originating at the bottom of the connection and extending toward one side of the specimen, as shown in figure 3.3(c). This crack represents the location real fatigue cracks are generated on the web gap near the girder-diaphragm connection in highway bridges. The second damage state (D2) was modeled by mirroring the first crack, as shown in figure 3.3(c), thus giving a total crack length of 50.8 mm.

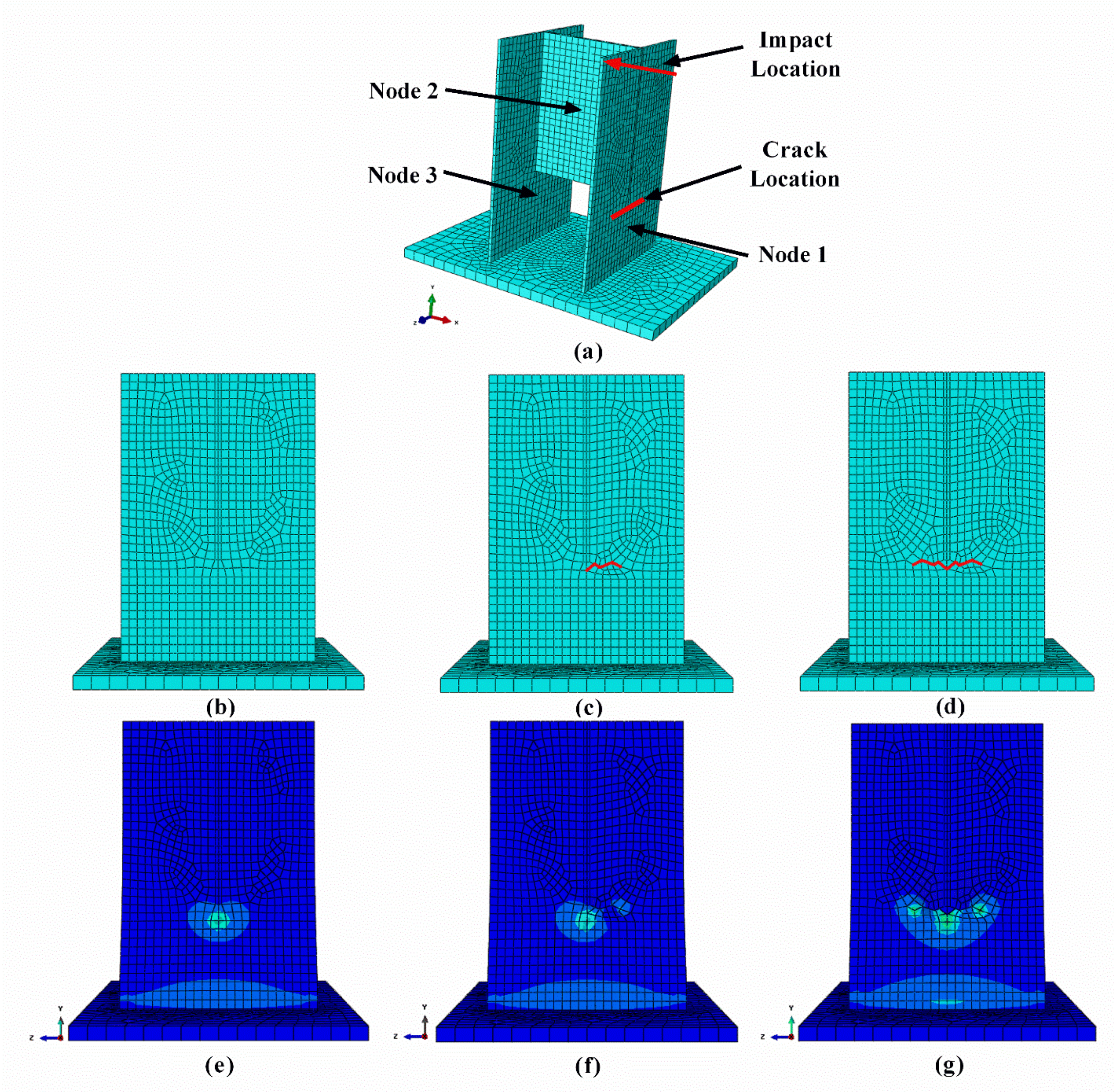

Figure 3.3 Numerical setup, crack location, and stress contour plots: (a) isometric view depicting crack, force, and node locations, (b) mesh for D0, (c) mesh for D1, (d) mesh for D2, (e) stress contour plot for D0 (red to blue = high to low stress), (f) stress contour plot for D1, (g) stress contour plot for D2

Typically in field applications, once a crack is detected, a retrofit is performed in order to prevent the crack from propagating further. A common retrofit is to drill a hole (stop-hole) at or near the crack tip(s) such that the stress concentration is relieved. While this measure does prevent the crack growth for many (but not all) of the scenarios, this project's purpose was to determine whether or not any crack forming after a retrofit could be detected. Therefore, 6.35 – 12.7 mm diameter holes were created at the crack tips of the numerical model with damage state D2, thus creating the retrofitted damage state D2H (where H specifies that there are stop-holes in the model). The size of these holes is the scaled dimension of the common 25.4 – 50.8 mm hole size used for retrofitting steel-girder highway bridges. The same analyses were repeated for additional damage states to determine if the damage detection algorithm of this work could detect the propagation of damage after a retrofit. The layout of the retrofitted numerical model is shown in Figure 3.4(a). Figure 3.4(b-d) depicts the meshing of the pseudo-girder web in which the crack was propagated for the retrofitted damage states (D2H, D3HA, and D3HB, respectively). Damage state D3HA represents cracks re-initiating through the "stop-holes," while damage state D3HB represents a crack branching from the initial retrofitted crack. D3HA was modeled by adding 6 mm seam cracks extending from the stop-hole. D3HB was modeled by a 25 mm jagged crack branching downward from the sharp notch in the middle of the existing crack. Figure 3.4(e-g) shows the respective stress contour plots for each of the damage states in figure 3.4(b-d), respectively, with the same color map used for the previous static analyses.

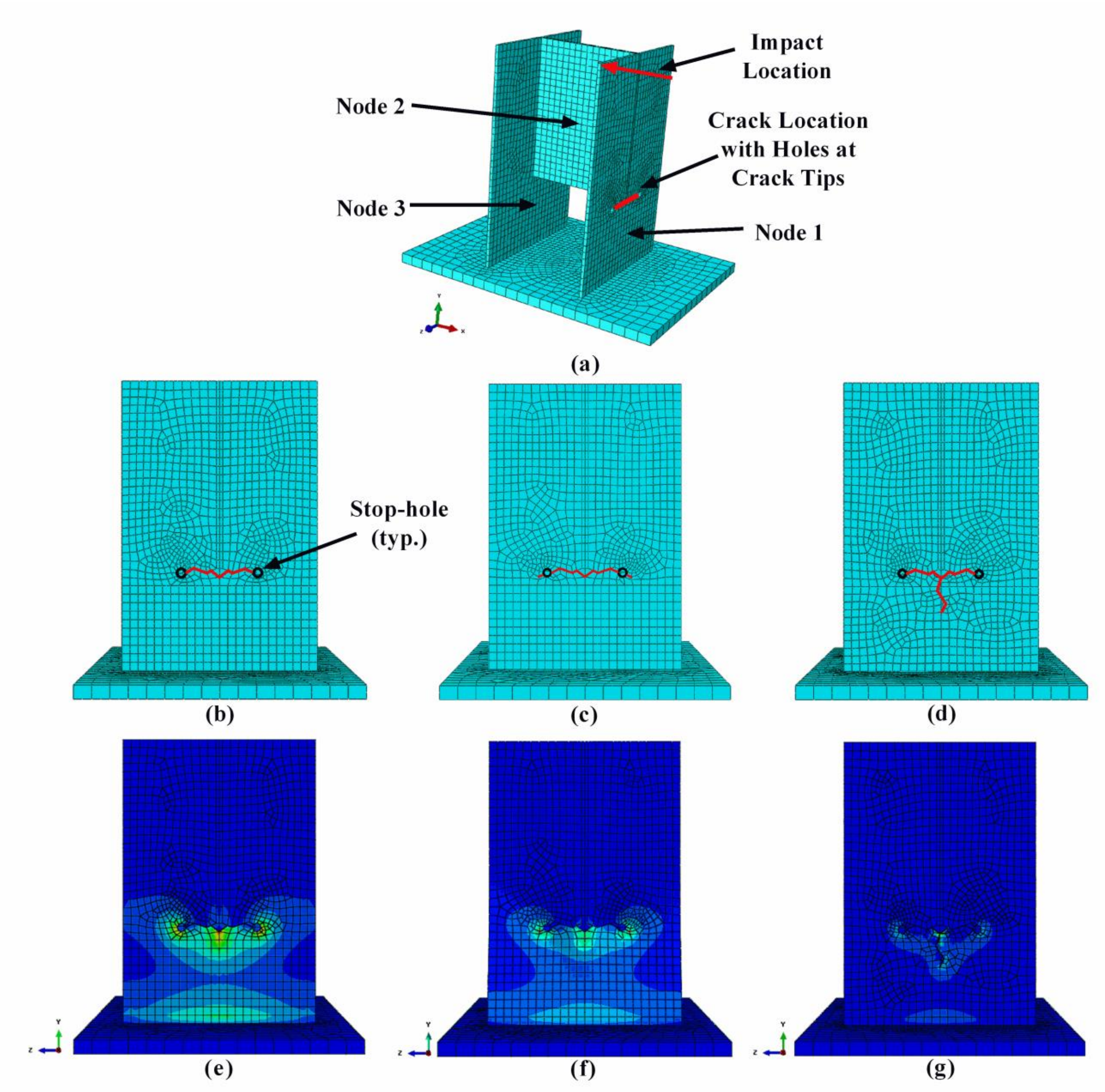

Figure 3.4 Numerical setup, crack location, and stress contour plots for retrofitted model: (a) isometric view depicting crack, force, and node locations, (b) mesh for D2H, (c) mesh for D3HA, (d) mesh for D3HB, (e) stress contour plot for D2H (red to blue = high to low stress), (f) stress contour plot for D3HA (g) stress contour plot for D3HB

3.1.2 Numerical Testing

An impact analysis was completed within Abaqus for each damage state such that the dynamic response of the system after an impact was monitored. A unit impact force was applied in the locations shown in figures 3.3 and 3.4 with a duration of 0.006 seconds, and the acceleration responses in the direction parallel to the loading at nodes 1, 2, and 3 (figs. 3.3 and 3.4) were measured before and after the impact, creating a 0.5 second time-history to be outputted to Matlab. An example of the acceleration time-history is shown in figure 3.5.

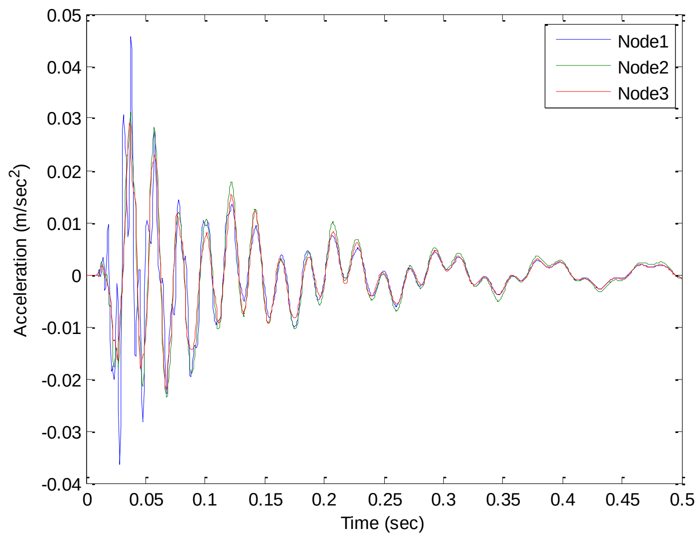

Figure 3.5 Acceleration time-histories from undamaged numerical model at nodes 1-3. Refer to figure 3.3(a) for node location.

Following the procedure of the damage detection algorithm, the acceleration time-histories were transformed into the frequency domain through a FFT, and **T** was calculated for symmetric pairs of nodes (2-1 and 2-3). The plots of transmissibility and how **T** changes with damage are shown in figure 3.6 for node pair 2-1, and figure 3.7 for node pair 2-3. It can be seen from these plots, specifically near 75 Hz and 150 Hz in figure 3.6, and near 150 Hz and 200 Hz in figure 3.7, that as damage increases, the frequency at which **T** peaks decreases. This is as expected in that the damage can be considered as a reduction in stiffness, and a reduction in stiffness is a reduction in the natural frequency of the system.

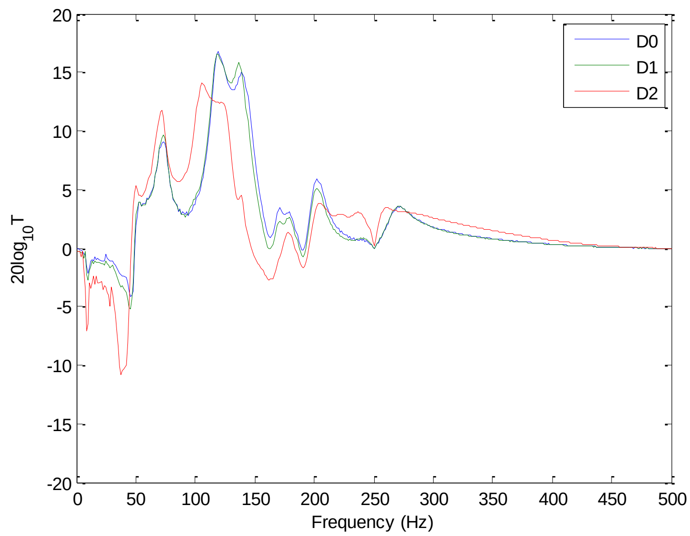

Figure 3.6 Transmissibility of numerical model for node pair 2-1 for non-retrofitted damage states (D0, D1, and D2)

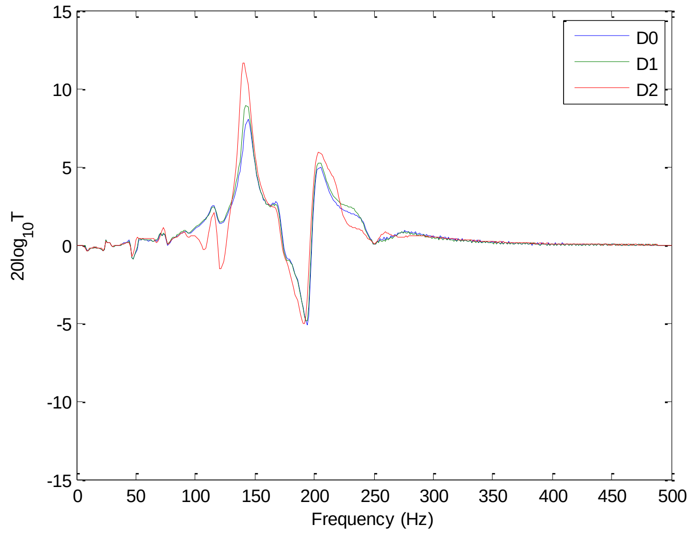

Figure 3.7 Transmissibility of numerical model for node pair 2-3 for non-retrofitted damage states (D0, D1, and D2)

Similar to the analysis conducted for the numerical model without holes, **T** was calculated for the same pairs of nodes for the damage states in which holes were created in the specimen (D2H, D3HA, and D3HB). The results of these calculations are shown in figure 3.8 for node pair 2-1 and figure 3.9 for node pair 2-3. The same trend can be seen: the peaks decrease in frequency as damage is increased, as shown near 100 Hz and 200 Hz in figure 3.8 and near 210 Hz in figure 3.9.

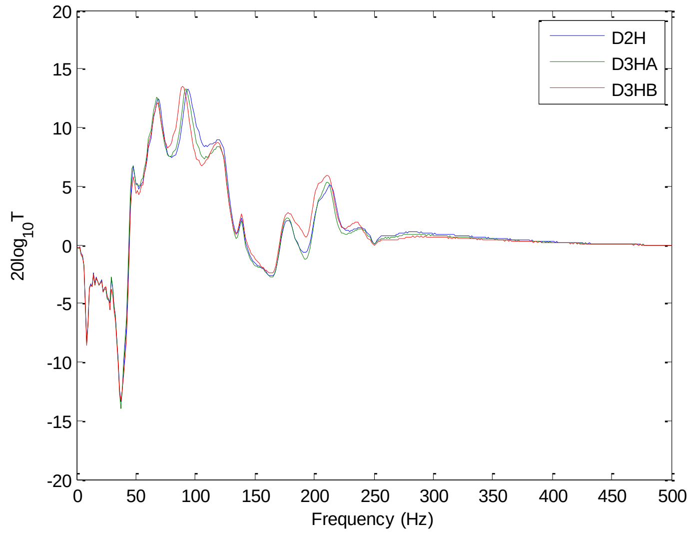

Figure 3.8 Transmissibility of retrofitted numerical model for node pair 2-1 for retrofitted damage states (D2H, D3HA, and D3HB)

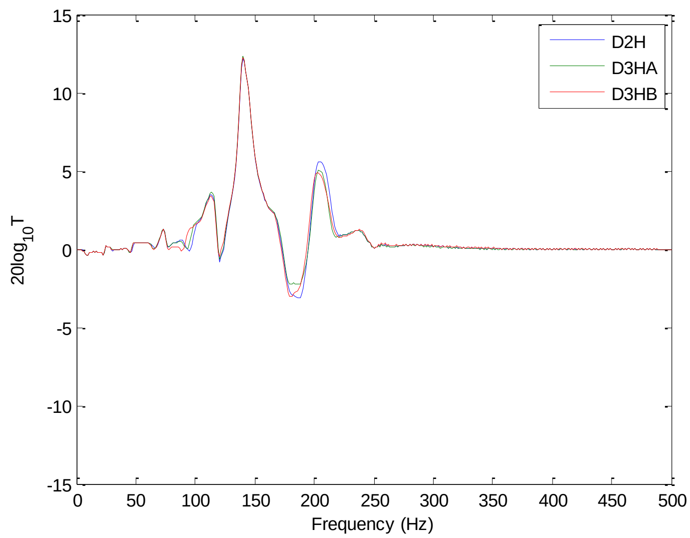

Figure 3.9 Transmissibility of retrofitted numerical model for node pair 2-3 for retrofitted damage states (D2H, D3HA, and D3HB)

A static analysis was conducted for each damage state to determine the stress concentrations within the model to verify the expected location of the crack. In this case, a 45 N static force was applied, similar to the impulse loading shown in figure 3.3(a), with the exception that the static force was applied at mid-span of the top of the pseudo-girder web in lieu of the dynamic force applied at the left edge of the top of the pseudo-girder web. This change in force location allowed for a symmetrical distribution of loading, thus eliminating any skewed stress contours caused by offsetting the load.

As shown in figure 3.3(e), a high stress concentration can be seen at the connection between the pseudo-girder web and diaphragm, thus justifying the expected location of crack initiation (Phares, 2013). This stress concentration remains for the first damage state (D1) [fig. 3.3(f)], as well as the second damage state (D2) [fig. 3.3(g)], justifying the location of crack propagation.

Additional static analyses were conducted for each retrofitted damage state to determine how the stress concentrations would change after retrofits were applied to a cracked specimen. The same static procedures as the non-retrofitted models were used. Since the static analysis shows that the retrofit introduces a higher stress concentration at the jagged vertex of the crack, the hypothesized scenario of crack propagation after a retrofit in this type of specimen under these loading conditions would be for the crack to branch. The third damage state (D3H) depicts this, as shown in figure 3.4(c).

3.1.3 Numerical Results and Discussion

By comparing the transmissibility with that of a baseline set of impacts (D0 for the damages states without holes and D2H for the damage states with holes), the damage indicator can be utilized to determine changes in the dynamic characteristics from the healthy state. As per the damage detection algorithm, the frequency range used in the damage indicator calculation was selected based on the coherence between the nodes, but since these analyses were completed numerically, the coherence is expected to be high across all frequencies (no noise or other uncertainties with the measurements); therefore, the range of frequencies used was set to 0-500 Hz based on the sampling frequency used for the analysis. The results for all the damage states of the specimen without holes (compared to the baseline D0) are shown in figure 3.10, and the results for the damage states of the specimen with holes (compared to the baseline D2H) are shown in figure 3.11.

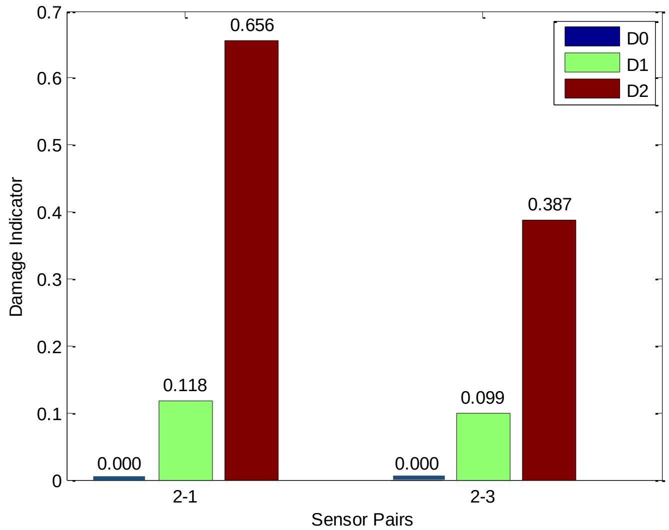

Figure 3.10 Damage indicator values of numerical analysis showing damage detection for numerical models without holes (D0, D1, and D2)

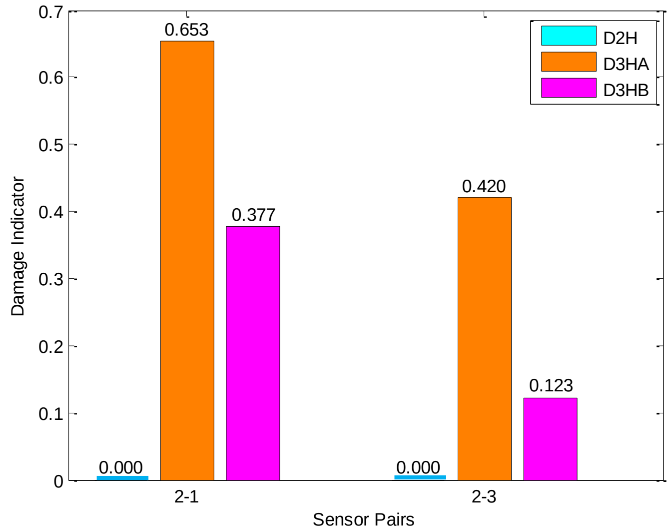

Figure 3.11 Damage indicator values of numerical analysis showing damage detection for numerical models with holes (D2H, D3HA, and D3HB)

From these results, it can be seen that damage is clearly detected for all damage states, as seen by the damage indicator values much greater than zero, and that no damage is detected for the baseline state when comparing to the respective baseline set of impacts, as seen by the damage indicator value of zero for D0 in figure 3.10 and D2H in figure 3.11. As depicted, the damage indicator for all damage states increases monotonically as damage increases, thus giving a relative quantification of the damage. It should be noted that figure 3.11 depicts two damage states that are not sequential (D3HA and D3HB), and the damage indicator may not increase monotonically between these two states. Also depicted in both figures is the trend that, even though the damage indicator detects damage for both pairs of sensors (since acceleration and transmissibility have both global and local sensing capabilities), the damage indicator is greater for the pair of nodes 2-1 than for 2-3, concluding that damage can be correctly located between nodes 2 and 1.

3.2 Laboratory Analysis

To validate the findings from the numerical analyses, an experimental investigation of the same connection specimen was conducted. The specimen was constructed with the same geometry as that of the numerical model shown previously in Figure 3.1 and fabricated from structural steel (AISI 1080). All connections were professionally welded to ensure that cracking due to external loading would occur in the plates of the specimen rather than in the welds.

3.2.1 Laboratory Setup

In this work, steel specimens with fatigue cracks and retrofitted fatigue cracks were tested and monitored under impact loading for crack re-initiation and growth. The layout of the experiments, including impact location and accelerometer placement, is shown in Figure 3.12. The specimen was impacted, using a force hammer with a rubber tip, at the specified location in order to measure the dynamic response of the specimen. For each damage case, twenty impacts were monitored to minimize the effect of uncertainties due to experimental noises and impact locations within the data collection.

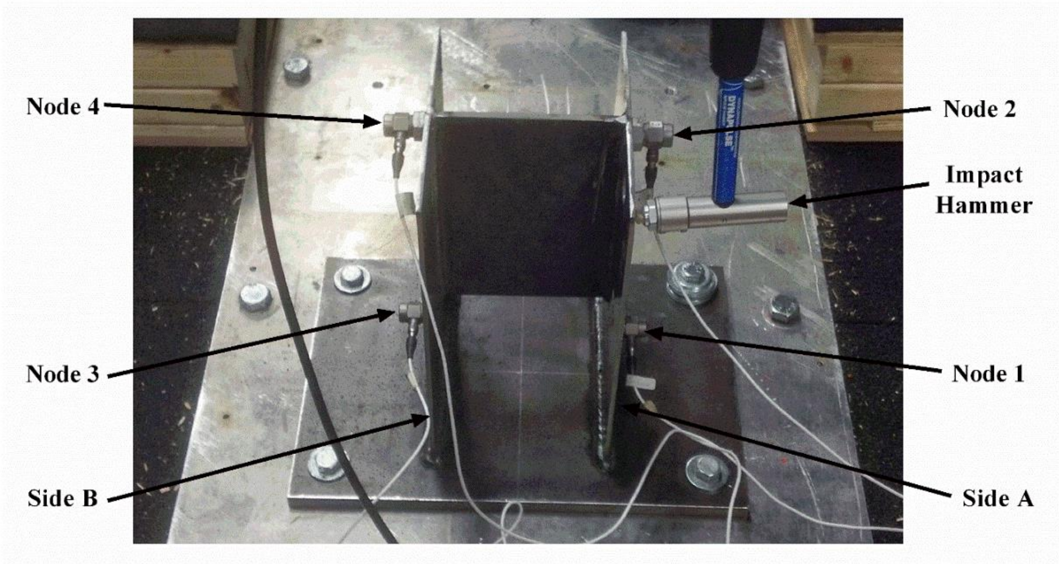

Figure 3.12 Experimental setup of specimen showing sensor and impact locations

Similar to the numerical analyses, multiple damage states were investigated to observe the damage detection capabilities of the algorithm for crack growth as well as crack re-initiation after a stop-hole retrofit. In order to create damage in these specimens, a variable-speed vibrating motor (shaker) (model SCR-200, VIBCO Inc.) that is capable of vibrating from 0-4000 rpm (0-67 Hz) and generating up to 890 N of force was attached to the specimen, thus vibrating the specimen at a specified frequency. In order to rigidly attach the shaker to the specimens, two 12.7 mm diameter holes were drilled to fit the shaker's bolts. Additional masses (four 2.25 kg masses) were clamped on the specimen in order to reduce the natural frequency of the specimen, thus allowing the shaker to vibrate around this adjusted natural frequency (thus causing an accelerated fatigue crack). The setup used for vibrating the specimen is shown in figure 3.13.

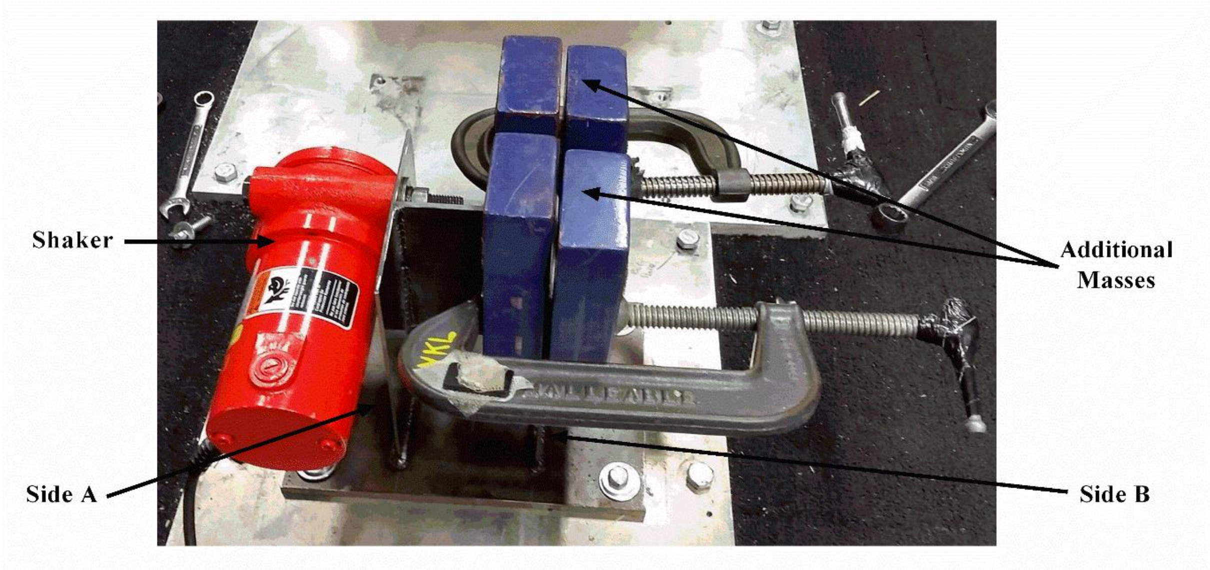

Figure 3.13 Experimental setup of specimen showing how damage was created, including the shaker attachment and additional mass location

For clarification of the damage locations (Figure 3.13), side A was the pseudo-girder web on which the shaker was attached (requiring bolt holes), and side B was the pseudo-girder web on which the additional masses were clamped. The crack was expected to form on side B near the connection of the pseudo-girder web and the pseudo-diaphragm, similar to the location depicted numerically in figures 3.3 and 3.4. Through conducting the experiments, however, it was noticed that while a crack did initiate in the expected region on side B, a crack was also initiated on side A. The crack on side A was caused by localized fatigue due to the shaker attachment.

3.2.2 Laboratory Testing

The testing procedure was similar to the numerical analyses completed in section 3.1.2 in that an impact test was conducted to measure the response of the system after an impulse load. To check for consistency in data collection and to verify the data processing results, a total of two specimens were fabricated and tested. The damage created by using the shaker for each specimen is shown in the respective subsections.

3.2.2.1 Specimen 1 - Testing

All of the damages created on side A of the specimen are shown in figure 3.14, and those for side B are shown in figure 3.15, along with an overall view of the respective side in which damage was observed.

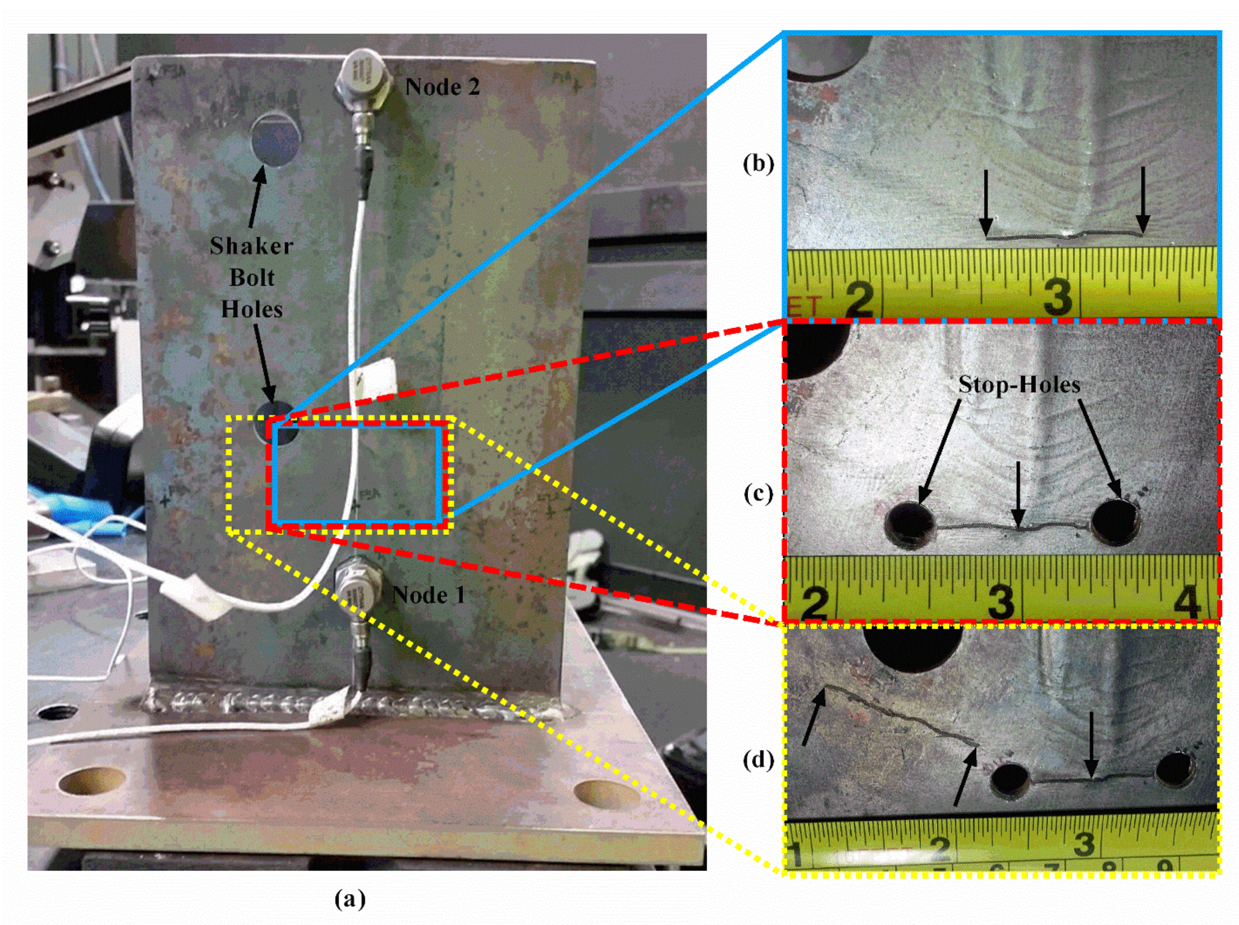

Figure 3.14 Damage caused in Specimen 1 - Side A: (a) overall side view indicating locations of damage, (b) 22 mm crack (D1), (c) 22 mm crack with 6.35 mm diameter holes drilled at crack tips (D1H), (d) 22 mm crack with 6.35 mm diameter holes drilled at crack tips and an approximately 25 mm crack originating away from the retrofit and propagating toward the existing crack (D2H)

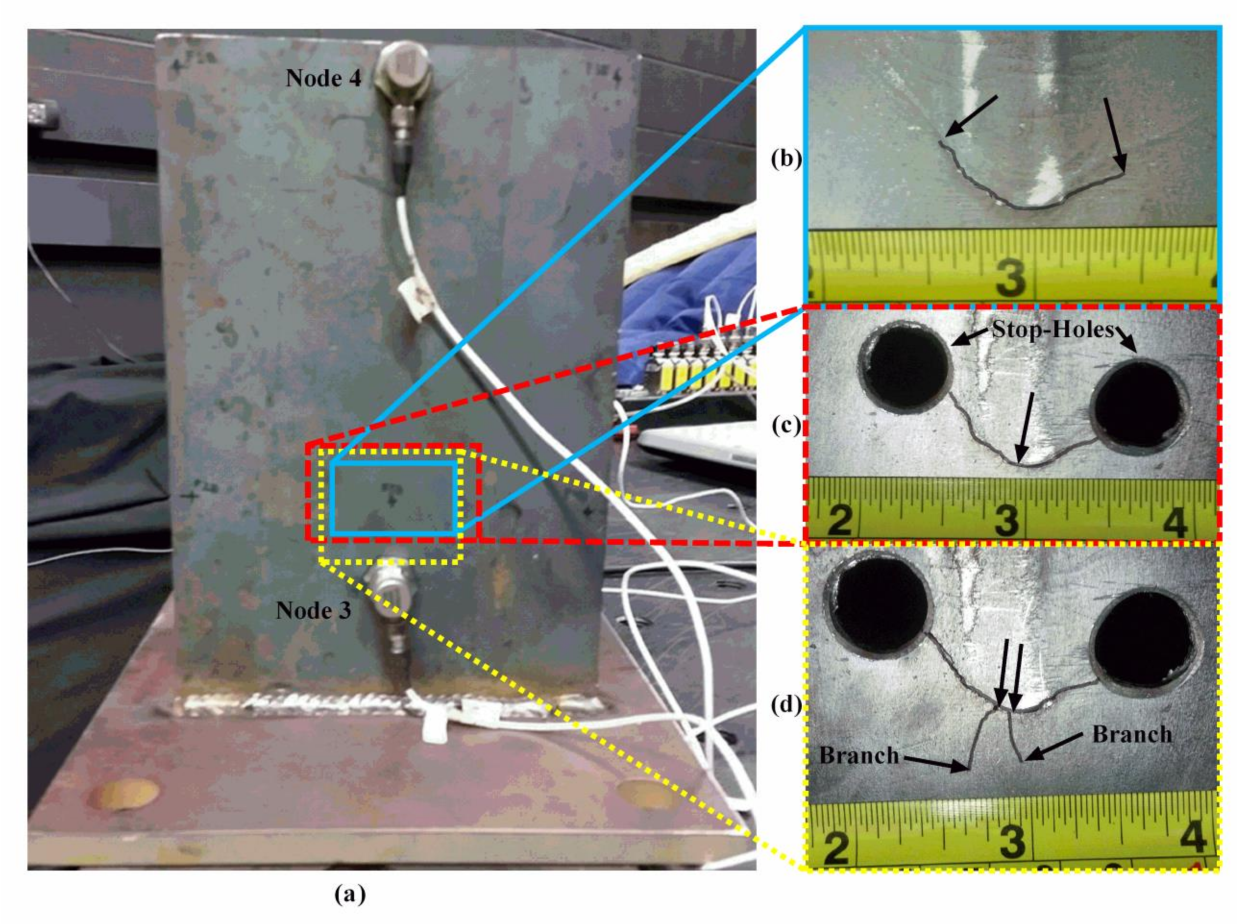

Figure 3.15 Damage caused in Specimen 1 - Side B: (a) overall side view indicating locations of damage, (b) 25 mm crack (D1), (c) 25 mm crack with 12.7 mm diameter holes drilled at crack tips (D1H), (d) 25 mm crack with 12.7 mm diameter holes drilled at crack tips and two cracks approximately 13 mm long branching from the middle of the existing 25 mm crack

The testing began by collecting the responses of twenty impacts for the undamaged specimen. The sensors were then removed to avoid breaking them during testing, and the shaker and additional masses were attached (fig. 3.13). By shaking the specimen near a natural frequency (approximately 53 Hz), large displacements were observed near the expected crack region. After five minutes of shaking at this resonance, a 22 mm crack was observed on side A of the specimen [fig. 3.14(b)], and a 25 mm curved crack was observed on side B [fig. 3.15(b)]. The shaker and masses were removed, and the sensors were replaced to monitor the response of this damage state (D1) by taking twenty more impacts. Stop-holes were drilled at the crack tips on both sides. Stop-holes 6.35 mm in diameter were drilled on side A, and 12.7 mm diameter stop-holes were drilled on side B to observe the effect of different size retrofits. Twenty impacts were monitored for this new baseline damage state (D1H), and damage was again propagated for the last damage state of this specimen (D2H). In damage state D2H, a second crack, 25 mm long, was observed on side A, originating near the connection point for the shaker and propagating toward the existing retrofitted crack [fig. 3.14(d)]. This crack was most likely caused by a high stress concentration as a result of the shaker being rigidly attached to the thin plate. In D2H, two cracks, each approximately 13 mm long, were observed branching from the middle of the retrofitted crack on side B [fig. 3.15(d)].

3.2.2.2 Specimen 2 - Testing

Using the same techniques as the first specimen, a second specimen was tested for verification of the results seen with specimen 1. All of the damages created on side A of the second specimen are shown in figure 3.16, and those for side B are shown in figure 3.17, along with an overall view of the respective side in which damage was observed.

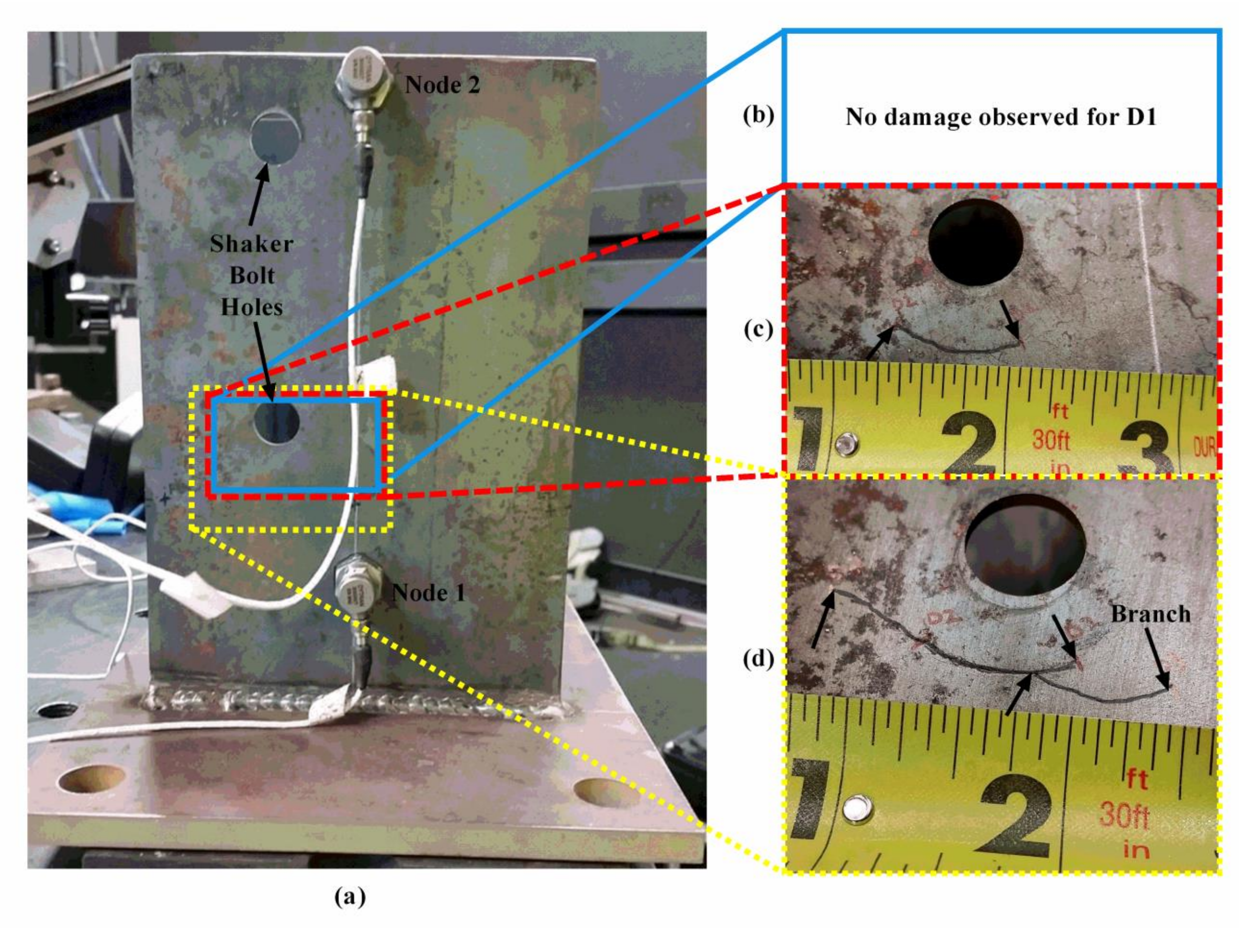

Figure 3.16 Damage caused in Specimen 2 - Side A: (a) overall side view indicating locations of damage, (b) no crack was observed (D1), (c) 19 mm crack (D2), (d) 32 mm crack with an approximately 19 mm crack branching from 6 mm in from the right crack tip (D3H)

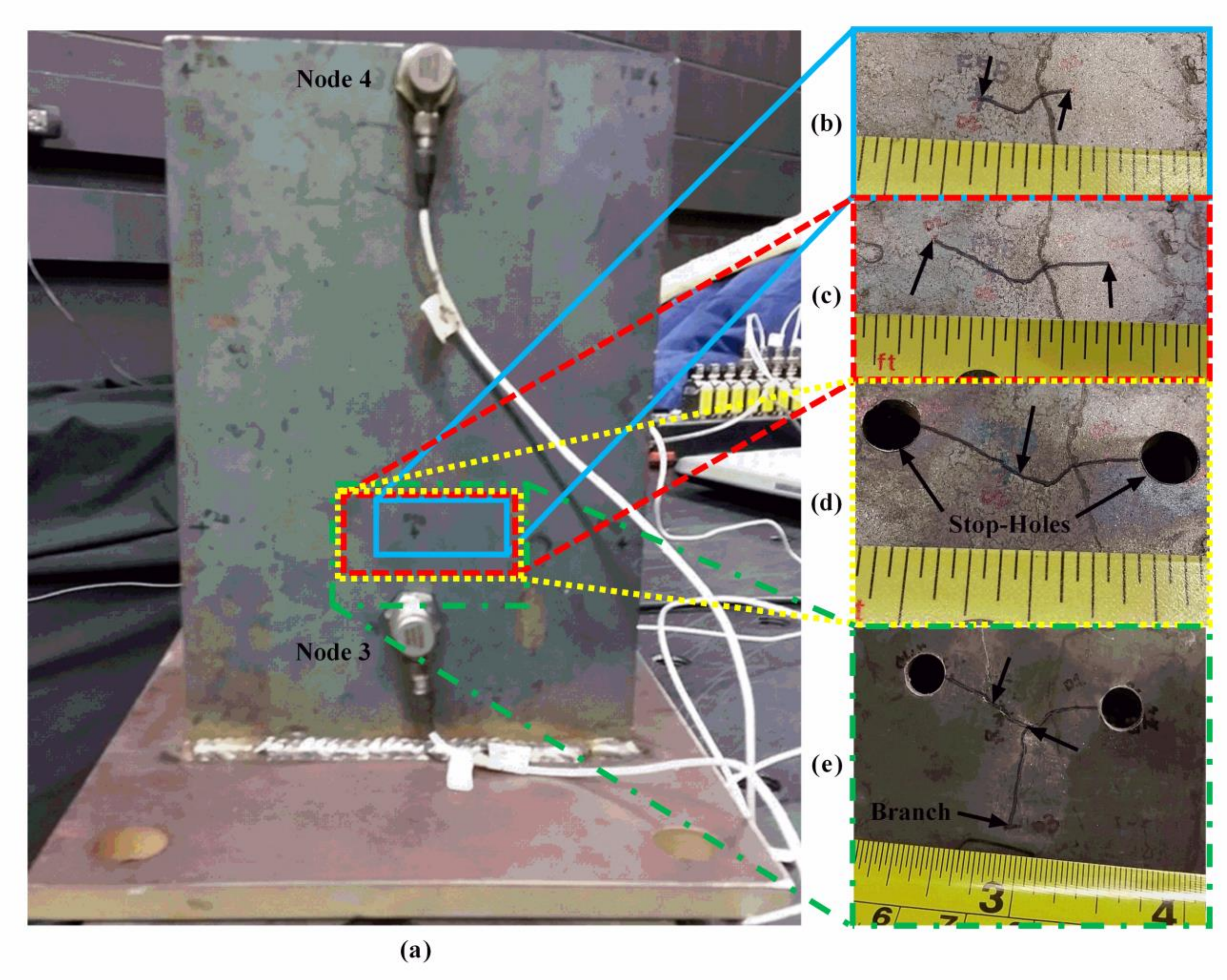

Figure 3.17 Damage caused in Specimen 2 - Side B: (a) overall side view indicating locations of damage, (b) 13 mm crack (D1), (c) 25 mm crack (D2), (d) 25 mm crack with 6.35 mm diameter holes drilled at crack tips (D2H), (e) 25 mm crack with 6.35 mm diameter holes drilled at crack tips and an approximately 13 mm crack branching from the middle of the 25 mm crack (D3H)

Firstly, the undamaged specimen was observed to obtain a baseline to be used for the damage detection algorithm. Damage was then introduced by attaching the shaker and masses and shaking the specimen around a natural frequency of the system. The first damage state (D1) for the second specimen had only a 13 mm crack on side B [fig. 3.17(b)] with no damage created on side A. Damage was then propagated for damage state D2, in which the crack on side B extended to a total of 25 mm long [fig. 3.17(c)], and a 19 mm crack began to form on side A [fig.

3.16(c)]. The crack on side A for this damage state was observed in a location near the shaker connection point, similar to the first specimen.

The specimen was then retrofitted with 6.35 mm diameter stop-holes to alleviate the stress concentration at the crack tips on side B (since the crack on side A was too close to the shaker attachment point to apply retrofits). The position of the holes with respect to the crack is shown in figure 3.17(d). After gathering a new baseline set of data for the retrofitted specimen (D2H), a third damage state was generated (D3H). The crack on side A propagated to a total length of 32 mm, with a 19 mm crack branching from it, approximately 6 mm from the right crack tip [fig. 3.16(d)]. It was observed that the same branching phenomena that occurred in the first specimen also occurred in the second, as there was a 13 mm crack branching from the middle of the retrofitted crack in side B [fig. 3.17(e)].

3.2.3 Laboratory Results and Discussion

With the observations seen by the propagation patterns, it can be suggested that, for this specimen and loading condition, the retrofit reduces the stress concentration at the crack tips of existing cracks; however, these retrofits do not alleviate the stress concentrations over the entirety of the crack, thus allowing for potential branching to occur. Throughout the experimentation, no crack was observed in which the crack re-initiated through the stop-hole.

To give an objective measure of the damage, the damage indicator for symmetric pairs of sensors were calculated; however, since an accelerometer could not be placed at a location similar to node 2 of the numerical study (fig. 3.3), the pairs of sensors analyzed were nodes 1-2 and 3-4, based on the sensor numbering shown in figure 3.12. The damage indicator results for each specimen are shown in their respective subsections.

3.2.3.1 Specimen 1 – Results

By taking the healthy state (BL-D0) as the baseline set of impacts used for the first analysis, figure 3.18 clearly shows that damage is not detected when comparing with additional impacts from the healthy state (damage indicator values of 0.001 and 0.002 for pairs 1-2 and 3-4, respectively). However, the damage indicator does detect damage for damage state D1 (damage indicator values of 0.447 and 0.515 for pairs 1-2 and 3-4, respectively). By observing that the magnitude of the damage indicator for D1 is larger between pair 3-4 than between pair 1-2, it can be deduced that a greater change in the dynamic characteristics of the specimen occurred between pair 3-4. This is consistent with the physical condition of the specimen, and therefore this observation gives rise to damage location within the algorithm.

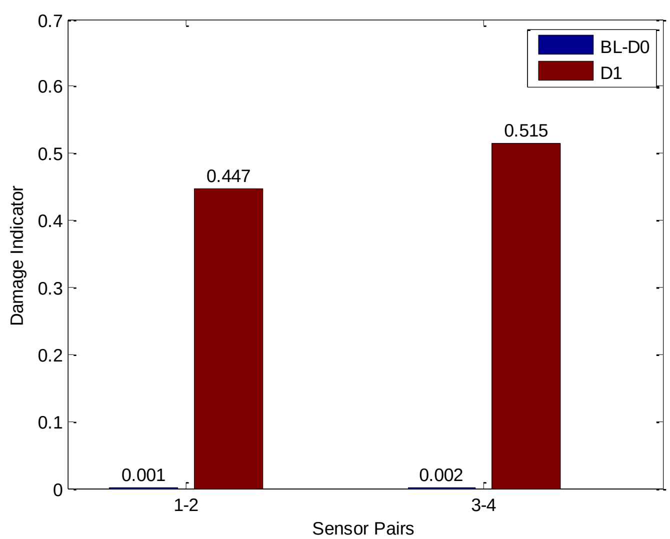

Figure 3.18 Damage indicator values of experimental analysis (specimen 1) showing damage detection for experimental models without holes (BL-D0 and D1)

After implementing the stop-hole retrofit to the first specimen, the system was monitored for use as the new baseline (BL-D1H). The results from the second analysis of the first specimen are shown in figure 3.19. Again, it can be seen that damage is not detected (0.001 for both pairs) when comparing with additional impacts from the baseline damage state (BL-D1H) and that damage is clearly detected (0.242 and 0.176 for pairs 1-2 and 3-4, respectively) for the damage state D2H. By applying the observation seen in the non-retrofitted analysis for comparative damage location, it is noticed that the magnitude of the damage indicator is greater between pair 1-2. By observing the magnitude of the damage that occurred in this damage state (figs. 3.14 and 3.15), the crack on side A (nearest pair 1-2) propagated more than the crack on side B (nearest pair 3-4), thus validating the observation that damage is comparatively located on side A.

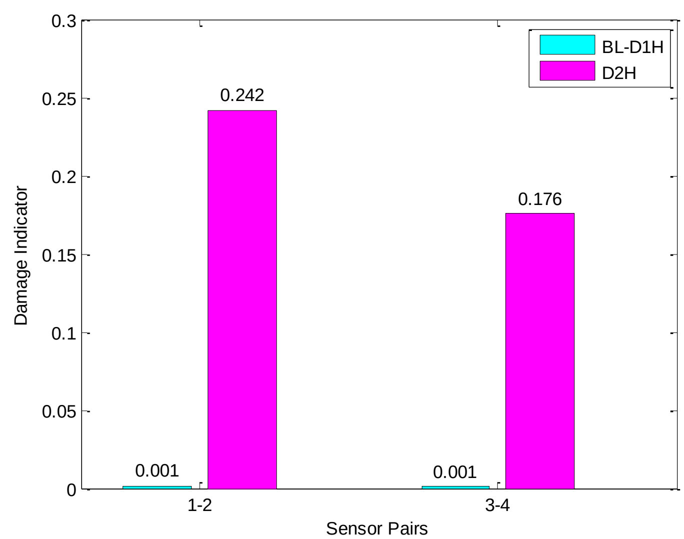

Figure 3.19 Damage indicator values of experimental analysis (specimen 1) showing damage detection for experimental models with holes (BL-D1H and D2H)

3.2.3.2 Specimen 2 - Results

By analyzing the responses of the second specimen using the same procedure as the first specimen, the damage indicator for the damage states before the retrofit (BL-D0, D1, and D2) are shown in figure 3.20, with the healthy state (BL-D0) taken as the baseline set of impact. The same trends observed with the first specimen are seen in these results in that damage is clearly detected for damaged states, not detected for additional impacts on the baseline state, and the damage is comparatively located based on the magnitudes of the damage indicators. An additional damage state was monitored for the non-retrofitted specimen 2 such that damage quantification could be investigated. Due to the complexity of the cracking, a specific quantification cannot be calculated; however, a relative quantification can be determined by observing the trend that the magnitude of the damage indicator increases monotonically as damage is propagated.

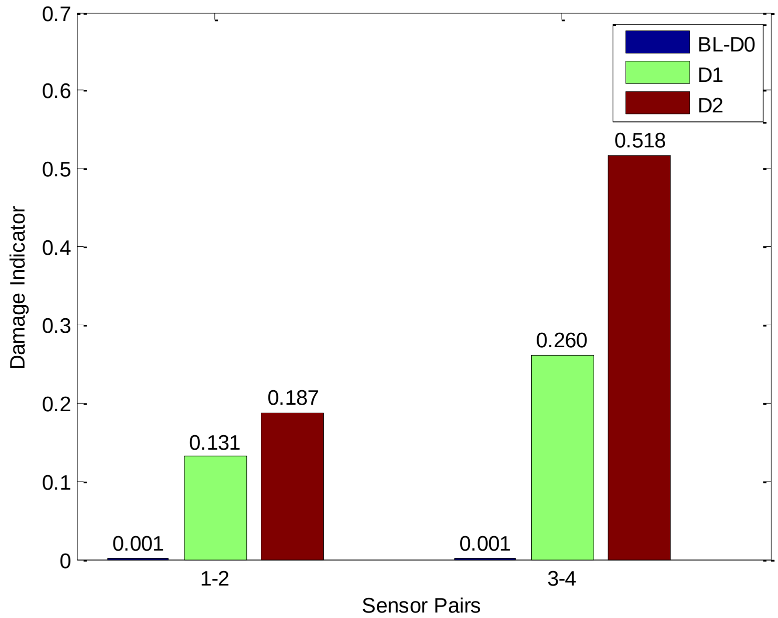

Figure 3.20 Damage indicator values of experimental analysis (specimen 2) showing damage detection for experimental models without holes (BL-D0, D1, and D2)

Figure 3.21 also shows these same trends for the retrofitted specimen, BL-D2H and D3H, excluding quantification due to the lack of additional damage states. Once more, the damage on side A of the specimen propagated further than the crack on side B during the last damage state; therefore, the magnitude of the damage indicator is greater between pair 1-2 than pair 3-4.

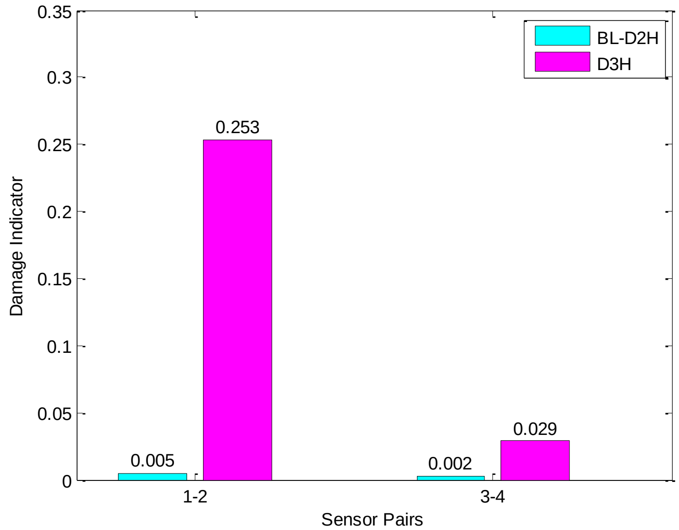

Figure 3.21 Damage indicator values of experimental analysis (specimen 2) showing damage detection for experimental models with holes (BL-D2H and D3H)

Chapter 4 Conclusion

Based on the observations from both the numerical and experimental analyses, it is concluded that the damage indicator can accurately detect, comparatively locate, and relatively quantify damage for regular damage states as well as retrofitted damage states. Damage is clearly detected for any damage state by observing the significant increase in the magnitude of the damage indicator. False damage is also correctly not detected when monitoring the baseline state as shown by the near zero values of the damage indicator, which are significantly lower than the values calculated from the damaged states. By comparing symmetric pairs of sensors, damage can be comparatively located by discerning the differences in the damage indicator. A greater magnitude of the damage indicator is caused by more significant changes in the dynamic characteristics of the structure. If the magnitude is larger on one side of the structure than on the other side, then damage is most likely occurring on the side with the higher magnitude, thus giving a comparative location to the damage. By this same principle, a relative quantification can be perceived in that the greater the change in the dynamic characteristics from the baseline, the greater the magnitude of the damage indicator. This relationship is monotonic, knowing that most damage cannot be undone within a structural system.

It should be noted that the laboratory experiments were limited by the fact that neither of the specimens were able to reproduce crack growth through a stop-hole. Even with this limitation, the presented algorithm proved successful in detecting fatigue crack initiation and propagation before retrofitting, as well as crack branching after retrofitting.

With potential field testing, the proposed damage detection methodology should be integrated with stochastic schemes to decrease the uncertainty resulting from random operational loading and environmental conditions.

References

Al-Emrani, Mohammad, and Robert Kliger. 2003. "FE analysis of stringer-to-floor-beam connections in riveted railway bridges." *Journal of Constructional Steel Research* 59, no. 7: 803-818.

Connor, Robert J., and John W. Fisher. 2006. "Identifying effective and ineffective retrofits for distortion fatigue cracking in steel bridges using field instrumentation." Journal of Bridge Engineering 11, no. 6: 745-752.

Chesné, Simon, and Arnaud Deraemaeker. 2013. "Damage localization using transmissibility functions: a critical review." *Mechanical systems and signal processing* 38, no. 2: 569-584.

Devriendt, Christof, and Patrick Guillaume. 2008. "Identification of modal parameters from transmissibility measurements." *Journal of Sound and Vibration* 314, no. 1: 343-356.

Doebling, Scott W., Charles R. Farrar, and Michael B. Prime. 1998. "A summary review of vibration-based damage identification methods." *Shock and vibration digest* 30, no. 2: 91-105.

Fisher, John W. 1997. "Evolution of Fatigue-Resistant Steel Bridges." *Transportation Research Record: Journal of the Transportation Research Board* 1594, no. 1: 5-17.

Grondin, G. Y., and G. L. Kulak. 2010. "Distortion-Induced Fatigue Cracking of Bridge Girders—Design Issues." In Structures Congress 2010, pp. 484-495. ASCE.

Johnson, Timothy J., and Douglas E. Adams. 2002. "Transmissibility as a differential indicator of structural damage." *Journal of Vibration and Acoustics* 124, no. 4: 634-641.

Li, Jun, and Hong Hao. 2013. "Damage Detection of Shear Connectors Based on Power Spectral Density Transmissibility." *Key Engineering Materials* 569: 1241-1248.

Liu, Ming, Dan M. Frangopol, and Kihyon Kwon. 2010. "Fatigue reliability assessment of retrofitted steel bridges integrating monitored data." *Structural Safety* 32, no. 1: 77-89.

Lu, Zizi, and Yongming Liu. 2010. "Small time scale fatigue crack growth analysis." *International Journal of Fatigue* 32, no. 8: 1306-1321.

Maia, Nuno M.M., Raquel A.B. Almeida, António P.V. Urgueira, and Rui PC Sampaio. 2011. "Damage detection and quantification using transmissibility." *Mechanical Systems and Signal Processing* 25, no. 7: 2475-2483.

Maia, Nuno M.M., António P.V. Urgueira, and Raquel A.B. Almeida. 2011. "Whys and wherefores of transmissibility." *Chapter* 10: 197-216.

Phares, Brent, Ping Lu, Terry Wipf, Lowell Greimann, and Junwon Seo. 2013. "Field Validation of a Statistical-Based Bridge Damage-Detection Algorithm." *Journal of Bridge Engineering* 18, no. 11: 1227-1238.

Tarries, David Joseph. 2002. "Diaphragm Bolt Loosening Retrofit for Web Gap Fatigue Cracking in Steel Girder Bridges." PhD diss., Iowa State University.

Thyagarajan, S. K., M. J. Schulz, P. F. Pai, and J. Chung. 1998. "Detecting structural damage using frequency response functions." Journal of Sound and Vibration 210, no. 1: 162-170.

United States Department of Transportation. 2013. Manual for repair and retrofit of fatigue cracks in steel bridges. FHWA Publication No. FHWA-IF-13-020.

Wipf, Terry J., L. F. Greimann, A. H. Khalil, and D. Wood. 1998. *Preventing cracking at diaphragm/plate girder connections in steel bridges*. No. Iowa DOT Project HR-393.

Wipf, Terry J., L. F. Greimann, B. Phares, and D. Tarries. 2003. *Retrofit methods of distortion cracking problems in plate girder bridges*. No. Iowa DOT Project TR-436.

Yan, Y. J., L. Cheng, Z. Y. Wu, and L. H. Yam. 2007. "Development in vibration-based structural damage detection technique." *Mechanical Systems and Signal Processing* 21, no. 5: 2198-2211.